Precipitation Cloud Identification Based on Faster-RCNN for Doppler Weather Radar

Yuanbo Ran
Fuling Meteorological Bureau
Haijiang Wang (whj@cuit.edu.cn)
https://orcid.org/0000-0002-3648-4225
Li Tian
Fuling Meteorological Bureau
Jiang Wu
Fuling Meteorological Bureau
Xiaohong Li
Liaocheng University

Research

Keywords: deep learning, precipitation clouds, Doppler Weather Radar Data, CAPPI, Faster-RCNN

Posted Date: November 6th, 2020

DOI: https://doi.org/10.21203/rs.3.rs-101255/v1

Version of Record: A version of this preprint was published on February 1st, 2021. See the published version at https://doi.org/10.1186/s13638-021-01896-5.

Precipitation Cloud Identification Based on Faster-RCNN for Doppler Weather Radar

Yuanbo Ran[1], Haijiang Wang[2*], Li Tian[1], Jiang Wu[1], Xiaohong Li[3]

1. Fuling Meteorological Bureau, Fuling, Chongqing 408000, China.

2. College of Electronic Engineering, Chengdu University of Information Technology, Chengdu, Sichuan 610225, China.

3. Physics Science and Information Engineering College, Liaocheng University, Liaocheng, Shandong, CO 252000, China.

* Corresponding author, e-mail: whj@cuit.edu.cn

Abstract

Precipitation clouds are visible aggregates of hydrometeor in the air that floating in the atmos-phere after condensation, which can be divided into stratiform cloud and convective cloud. Different precipitation clouds often accompany different precipitation processes. Accurate identification of precipitation clouds is significant for the prediction of severe precipitation processes. Traditional identification methods mostly depend on the differences of radar reflectivity distribution morphology between stratiform and convective precipitation clouds in three-dimensional space. However, all of them have a common shortcoming that the radial velocity data detected by Doppler Weather Radar has not been applied to the identification of precipitation clouds because it is insensitive to the convective movement in the vertical direction. This paper proposes a new method for precipitation clouds identification based on deep learning algorithm, which is according the distribution morphology of multiple radar data. It mainly includes three parts, which are Constant Altitude Plan Position Indicator data (CAPPI) inversion for radar reflectivity, Radial projection of the ground horizontal wind field by using radial velocity data, and the precipitation clouds identification based on Faster-RCNN. The testing result shows that the method proposed in this paper performs better than typical existing algorithms in terms of accuracy rate. Moreover, this method boasts great advantages in running time and adaptive ability.

Keywords: deep learning; precipitation clouds; Doppler Weather Radar Data; CAPPI; Faster-RCNN

1 Introduction

In recent decades, the precipitation clouds identification based on ground-based weather ra-dar detection data, has been widely used in radar quantitative precipitation estimation, weather modification, and aviation meteorology. The capability of microwaves to penetrate cloud and rain has placed the weather radar in an unchallenged position for remotely surveying the atmosphere [1-3]. Doppler weather radar, referred as a greatest tool for detecting weather processes, can not only detect the distribution of precipitation clouds in the atmosphere, but also detect the move-ment trend of precipitation clouds [4-6].

In earlier research, the zero-layer bright band is mostly used as the basis for the identification of precipitation cloud types. For the region with the phenomenon of the zero-layer bright band, the precipitation clouds type defaults to stratiform cloud; otherwise it is convective cloud [7]. The limitation of these methods is that the zero-layer bright band is visible only when the stratiform cloud precipitation develops to maturity. Houze et al. [8] proposed a method to distinguish the precipitation cloud types by using rainfall gauge measurement data. When the precipitation intensity exceeds a certain fixed threshold, the precipitation cloud is considered as convective cloud; otherwise, it is stratiform cloud. The limitation of this method is that it can only determine the center of convective cloud, and it is easy to misjudge the precipitation area of convective cloud with weak precipitation intensity nearby. Churchill et al. [9] determine the convective cloud center through the radar reflectivity threshold. Moreover, precipitation clouds within a fixed radius of the convective cloud center are all convective clouds by default, otherwise they are stratiform clouds. Steiner et al. [10] pointed out the irrationality of using reflectivity threshold and influence radius to determine convective cloud region. The reflectivity threshold of the convective cloud center should be determined according to the reflectivity distribution of the region near the convective cloud center, and the influence radius should be calculated by the reflectivity of the convective cloud center. The limitation of these methods is that they do not take into account the influence of the zero-layer bright band, which leads to misdiagnosis of stratiform clouds as convective clouds. Biggerstaff et al. [11] analyzed the distribution of radar reflectivity corresponding to stratiform and convective cloud in three-dimensional space, and applied it to the identification of precipitation clouds. This method takes into account the influence of zero-layer bright band and

achieves good recognition results. Therefore, this method has been widely used in the United States. In Reference [12], the authors proposed a method to distinguish the precipitation cloud types based on the difference of radar reflectivity distribution morphology between convective and stratiform precipitation clouds. In this paper, six preparative reflectivity-morphological parameters are presented, which are composite reflectivity and its horizontal gradient, echo top height associated with 35 dBZ reflectivity and its horizontal gradient, vertically integrated liquid water content and its density. Moreover, the precipitation clouds are identified by using the fuzzy logic algorithm based on the distribution of each reflectivity-morphological parameter. The accuracy of these methods depends on the reliability and quantity of the selected parameter. However, the increment of identification parameters leads to the multiplication of computation, which causes the great reduction of the efficiency of the algorithm.

All of the above methods are based on the reflectivity data, which are detected by Doppler weather radars. However, the radial velocity data detected by Doppler Weather Radar has not been applied to the identification of precipitation clouds. It is due to the radial velocity of the radar is the velocity of the precipitation particle relative to the radar, which is not sensitive to the convection movement in the vertical direction [13, 14]. In the present study, we propose a new method for precipitation clouds identification based on the deep learning algorithm. Firstly, the adaptive Barnes interpolation method is used to interpolate the radar scanning volume data to obtain the reflectivity CAPPI data at multiple altitudes. Secondly, the radial velocity data of the ground horizontal wind field is inversed by using the radial velocity data detected by Doppler weather radar at minimum elevation. Finally, the Faster-RCNN model is applied to identify the precipitation clouds based on the result above mentioned.

This paper is organized as follows: Section 2 describes the Datasets for deep learning training and testing. Section 3 presents the new method for precipitation clouds identification based on Faster-RCNN algorithm. Section 4 evaluates the proposed method by comparing the identification results with the traditional method. Section 5 concludes this study.

2 Data

In this research, we collected a large amount of precipitation data from the CINRAD-SA dual-polarization Doppler weather radar, which is located in Guangzhou, Guangdong, China

(23°01′N, 113°35′E). The radar characteristics are shown in Table 1.

Table 1 The characteristics of CINRAD-SA radar

Antenna	Type	Parabolic
	Beam width	Horizontal 0.95° Vertical 0.95°
	Scan type	PPI、RHI、VOI
	Polarization	Horizontal or vertical
	Gain	45dB
Transmitter	Frequency	2885M HZ - S band
	Power	650-800KW
	Pulse width	1.57us
Receiver	processing mode	PPP/FFT
	Noise figure	~4 dB
	Dynamic range	> 94dB
Variables Available	Reflectivity, Radial velocity, Spectral width, Differential reflectivity、Copolar correlation coefficient, Differential propagation phase constant, Linear depolarization ratio, and so on.	

Table 2 The datasets used in the experiments

Set	Data	Size	Origin(0°)	90°	180°	270°	Total
Training	Z-CAPPI	(400,400,5)	1600	1600	1600	1600	6400
	V-Projection	(400,400)	1600	1600	1600	1600	
	W-Projection	(400,400)	1600	1600	1600	1600	
Testing	Z-CAPPI	(400,400,5)	200	200	200	200	800
	V-Projection	(400,400)	200	200	200	200	
	W-Projection	(400,400)	200	200	200	200	

In this paper, Faster-CNN algorithm is adopted to identify the precipitation clouds, which is a target detection algorithm based on convolution neural network (CNN). The accuracy of the final identification result depends on the number of sample sets in the training process. In order to obtain high accuracy of precipitation clouds identification, this paper constructs a rich sample set, which including 6400 training samples and 800 test samples. Table 2 summarizes the datasets used in this paper. As shown in Table 2, each sample is a matrix with a size of $400\times400\times7$ cells, and it can be divided into three parts, which are reflectivity data (Z) after CAPPI inversion; the radial velocity data (V) and spectral width data (W) of the ground horizontal wind fields, which are inversed by using the radar detection data at minimum elevation.

3 Methods

3.1 The CAPPI Inversion of Reflectivity

The rainfall measurement of dual polarization weather radar is based on the basis that the raindrops in the process of falling are not spherical but have an oblate spheroidal shape, and the shape is determined by the equivalent diameter and axis ratio. The axis ratio b/a, the ratio of the major axis length to minor axis length, is related to the diameter D_e of an equivalent-volume spherical raindrop as [9].

The stratiform cloud is caused by the vertical rising movement of the air in a wide range. Moreover, the rising velocity is uniform and often less than the falling velocity of raindrops. In generally, stratiform cloud is larger in horizontal scale, thinner in vertical thickness, and has flat tops [15, 16]. During the radar detection, the characteristics of stratiform cloud in reflectivity data can be summarized as follows. a) The reflectivity data are uniformly distributed and have a diffuse shape. In the process of large-scale stratiform cloud precipitation, there may be multiple reflectivity centers, but the value of reflectivity center generally does not exceed 30dbZ. b) The horizontal and vertical gradients of reflectivity data are small. c) It is often accompanied by the phenomenon of the zero-layer bright band when surface precipitation particles are liquid.

The convective cloud is caused by the air vertical movement due to the instability of the atmosphere. Its horizontal scale is small, and the vertical convection is strong, often accompanied by storm, rainstorm, hail, and other disastrous weather [17]. During the radar detection, the characteristics of convective cloud in reflectivity data can be summarized as follows. a) The reflectivity value of the convective cloud is larger than stratiform cloud, and the central reflectivity value can reach above 50dbZ. b) The horizontal and vertical gradients of reflectivity data are large.

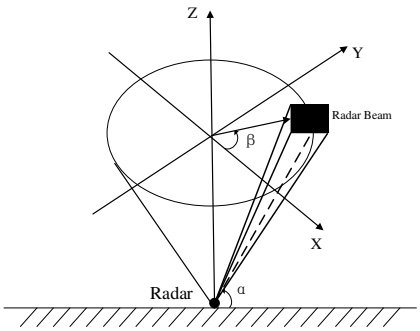

Fig. 1 The schematic diagram of PPI scan mode

In china, the main operational radar of China Meteorological Administration is Doppler weather radar, which can not only obtain the distribution information of precipitation particles in atmosphere, but also provide the information of the atmospheric wind field. During the Doppler weather radar operation process, VCP21 working mode is a common choice for meteorological service. It can complete a volume scan in 6 minutes, and each volume scan consists of 9 elevations. For each elevation, the Plane Position Indicator (PPI) scan mode is adopted. As shown in Fig. 1, the radar antenna captures precipitation data in the atmosphere in a fixed elevation, omni-directional scanning mode, and in polar coordinates (radar-centered) with different color scales to indicate the magnitude and direction of the values. This scanning method is called PPI scanning. In other words, radar can acquire the information of precipitation particles in a three-dimensional space in 6 minutes, which provides guarantee for the real-time prediction in weather operation. In the process of identifying the precipitation cloud, in order to describe the vertical and horizontal characteristics of the precipitation cloud system more intuitively, the PPI data of all elevations need to be processed through spatial interpolation to obtain the information of the precipitation particles at a certain altitude, namely CAPPI data.

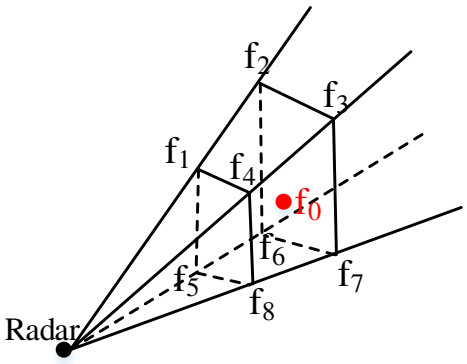

Fig. 2 An illustration of Adaptive Barnes interpolation.

Adaptive Barnes interpolation is a commonly used interpolation method, which is mainly used in discrete point interpolation with sparse distribution [18, 19]. As shown in Fig. 2, where f_1 ~ f_8 are values detected by radar in 8 range bin, f_0 is the point that needs to be interpolated. The interpolation method can be expressed as

$$f_0 = \frac{\sum_{k=1}^{8} \omega_k \times f_k}{\sum_{k=1}^{8} \omega_k} \tag{1}$$

Where, ω_k is the weight of f_k, which can be defined as

$$\omega_k = \begin{cases} \exp\left[-\frac{(r_k - r_0)^2}{K_r} - \frac{(\theta_k - \theta_0)^2}{K_\theta} - \frac{(\phi_k - \phi_0)^2}{K_\phi} \right] & (f_k \ is \ valid) \\ 0 & (f_k \ is \ invalid) \end{cases} \tag{2}$$

Where, r_k, θ_k and ϕ_k are distance, azimuth and elevation in polar coordinates corresponding to f_k respectively. Assuming that the coordinate of f_0 in cartesian coordinate system is (X_0, Y_0, Z_0), and the radar station is the origin of coordinates by default, then the polar coordinate (R_0, θ_0, ϕ_0) corresponding to f_0 can be expressed as

$$\begin{cases} R_0 = \sqrt{X_0^{\ 2} + Y_0^{\ 2} + Z_0^{\ 2}} \\ \theta_0 = \arctan(Y_0 / X_0) \\ \phi_0 = \arctan(Z_0 / \sqrt{X_0^{\ 2} + Y_0^{\ 2}}) \end{cases} \tag{3}$$

In equation 2, K_r, K_θ and K_ϕ are smoothing parameters of radial distance, azimuth and elevation respectively, which can be adjusted to achieve different smoothing effects. In this paper, $K_\theta = 0.76$, while K_r and K_ϕ can be defined as

$$K_r = R^2 \times K_\theta \tag{4}$$

$$K_\phi = \cos^2 \phi \times K_\theta \tag{5}$$

The resolution of radar data in radial distance, azimuth and elevation is different during interpolation. In the radial direction, the distance between adjacent range bins is fixed. In the direction of azimuth, the distance between adjacent range bins increases with the increase of radial distance. Moreover, in the elevation direction, the distance between adjacent range bins increases with the increase of radial distance. Therefore, different interpolation points have different dependencies in three directions, so it is necessary to set smoothing parameters according to the dependencies in three directions [34]. Compared with the traditional interpolation method for CAPPI inversion, the Adaptive Barnes interpolation method has better smoothing effect.

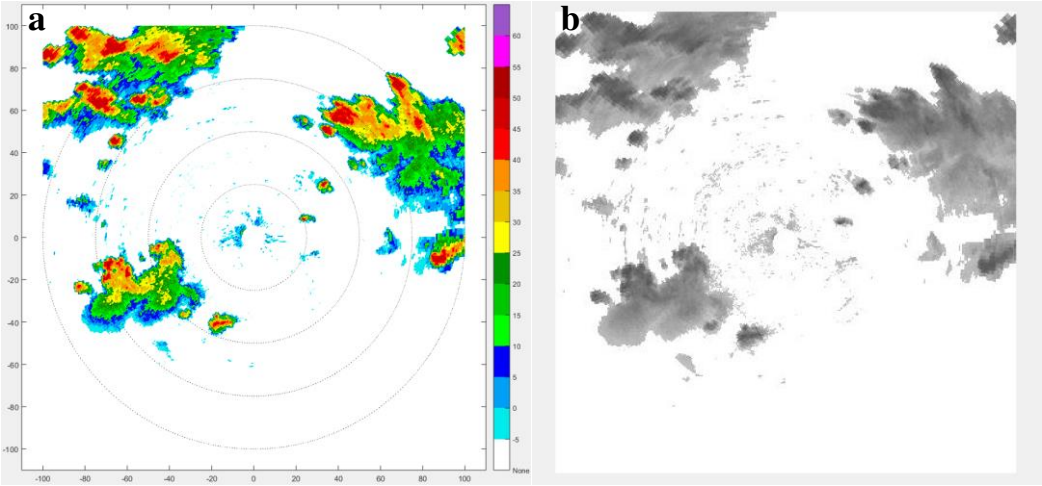

Fig. 3 Standardization of radar reflectivity CAPPI data, **a** origin, **b** Standardization

The inputs of the deep learning algorithms are mostly the data after standardization. Before using the Faster-RCNN model to identify the precipitation clouds, the paper needs to conduct a standardized processing on the reflectivity data. Fig. 3(a) is the CAPPI distribution diagram of reflectivity data at a height of 2 km, which corresponds to a reflectivity data matrix with a size of 400×400 cells. Fig. 3(b) is the distribution diagram of reflectivity matrix after standardization, which can be summarized as

$$\begin{cases} \bar{X} = \dfrac{X - X_{Min}}{1.2\times(X_{Max} - X_{Min})} + 1/6 \\ \bar{X} = 0 \qquad (X \ is \ \text{Null}) \end{cases} \tag{6}$$

Where, X is the input to the normalized function, and $\bar{X}$ is the output after standardization.

3.2 Radial projection of ground horizontal wind field

As the name suggests, convective cloud have strong convective phenomena in the vertical direction, which should be an important basis for judging convective cloud. However, the velocity data detected by the Doppler weather radar is the relative velocity of cloud particles in the radial direction, and it is not sensitive to the convective motion in the vertical direction, so it is difficult to apply this feature to the identification of precipitation clouds. Convective clouds usually consist of one or more convective cells, each of which has a horizontal scale ranging from several kilometers to tens of kilometers. In radar reflectivity maps, convective cells are usually marked by a tight reflectivity region or a strong updraft that causes deep convection [20]. As shown in Fig. 4, the evolution process of convective cells usually includes three stages: growth stage, mature stage,

and disappearing stage [21].

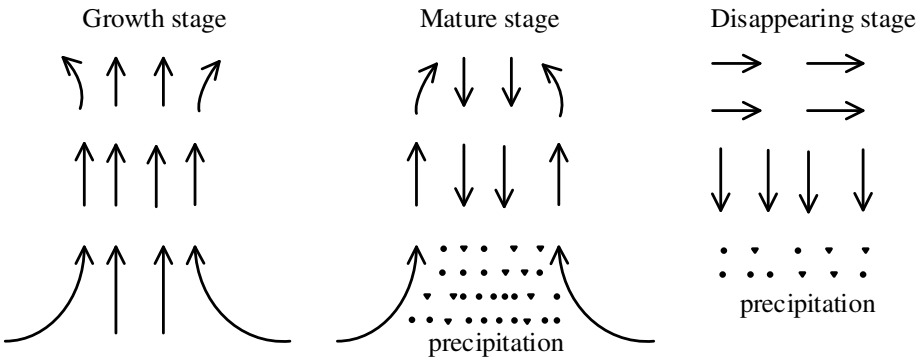

Fig. 4 The evolution process of convective cells

As shown in Fig. 4, the convective cells growth stage is mainly controlled by the updraft, and the rising velocity of updraft increases with the height. The updraft is mainly caused by the convergence of surface air, which is shown in Fig. 5 (a). The mature stage of convective cells is the coexistence stage of updraft and downdraft. In this stage, the updraft in the cloud reaches the maximum, and the downdraft is mainly caused by the falling of precipitation particles. Moreover, the downdraft diffuses continuously from the convective cloud center to the periphery, forming the precipitation in a large area. The ground divergence field is shown in Fig. 5 (b). The disappearing stage of convective cells is mainly controlled by the downdraft. Precipitation at the bottom of the cloud will become weaker and weaker, and the airflow at the top of the cloud will be dominated by horizontal advection.

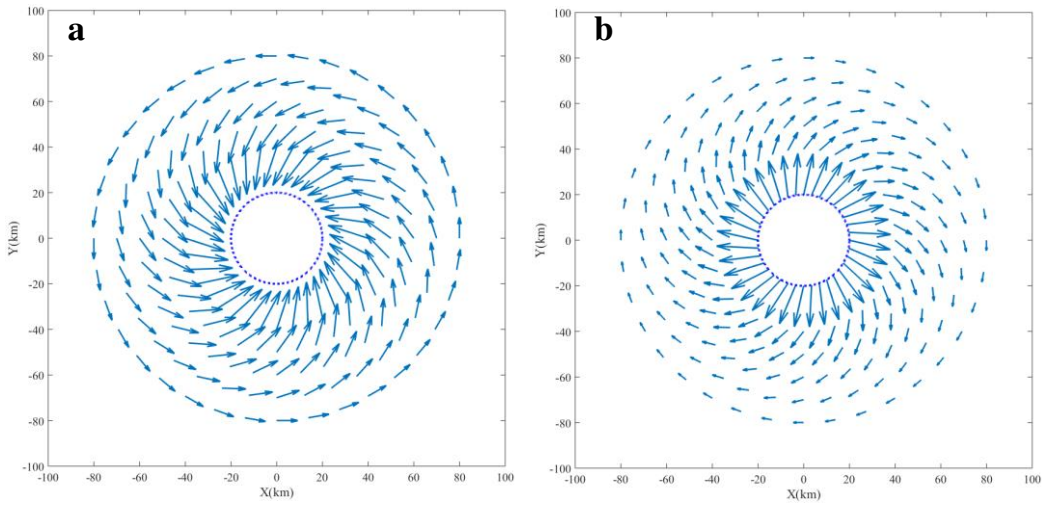

Fig. 5 Simulation diagram of ground wind field, **a** convergence, **b** divergence

In order to understand the distribution of convergence and divergence in the radial direction

of radar, same scale cyclones were simulated in four directions of the radar station, which are projected into the radial velocity map corresponding to the 0.5° elevation. Fig. 6(a) shows the PPI distribution of radial velocity corresponding to the convergence wind field. As shown by the cyclone due north, the radial velocity of the left region is negative, and the right side is positive. The radial velocity of the convergence field gradually increases from the outside to the inside, and suddenly becomes zero at the center of the convergence field, which is mainly caused by the uplift of the convergent airflow. Moreover, the convergence field has obvious zero velocity line at the boundary of positive and negative velocity. In addition, the PPI distribution of radial data corresponding to the divergence wind field is shown in Fig. 6(b).

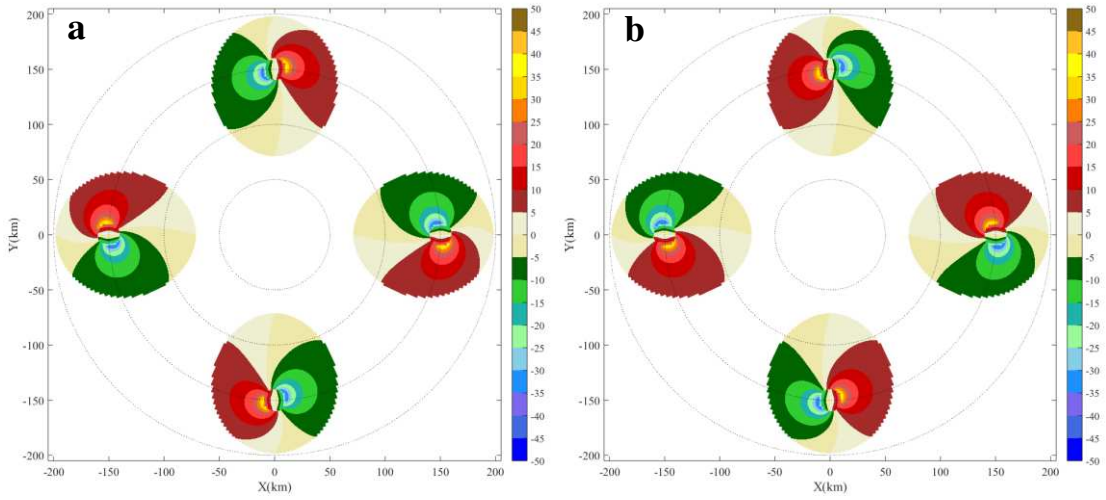

Fig. 6 The PPI distribution of the radar radial velocity data corresponding to **a** convergence and **b** divergence

As mentioned above, in the growth and maturity stages of convective cells, the ground wind field is accompanied by convergence and divergence, which has obvious distribution characteristics in the radial velocity data detected by the radar at the minimum elevation. Moreover, the minimum elevation of Doppler weather radars is usually less than 0.5°, and the vertical component of the radial velocity detected by the minimum elevation is close to zero. Therefore, the radial velocity detected by the minimum elevation can be regarded as the projection of horizontal wind field on the radar radial direction. In order to maintain the consistency of the radial velocity data and the reflectivity CAPPI data in spatial distribution, this paper projected the radial velocity data into the horizontal surfaces, and took it as the radial velocity data of the ground horizontal wind field.

The spectral width of the radial velocity data is an important Doppler weather radar data product, which reflects the dispersion of the radial velocity data in a range bin. Moreover, it is proportional to the variance of the velocity vectors of each scatterer in the range bin. In the convergence and divergence field, the distribution of velocity vectors in the range bin is usually chaotic, so it usually has a large spectral width. Therefore, the spectral width of the radar radial velocity data should be applied to identify the precipitation clouds. In this paper, the radial velocity data and spectral width data corresponding to the ground wind field is obtained by the projection of the radar detection data at the minimum elevation. As shown in Table 2, the size of radar radial data and spectral width data corresponding to the ground wind field is 400×400 .

3.3 The identification of precipitation clouds base on Faster-RCNN

In recent years, deep learning has developed rapidly, and the target detection method based on deep learning has achieved good results. References [21] to [33] describe the achievements of deep learning in target detection. The deep learning algorithm has strong self-learning ability and can extract features from the original input data, which reflect the structural information of the input data. Therefore, compared with the traditional target detection algorithm, the target detection methods based on deep learning have more advantages in accuracy and efficiency. Moreover, the emergence of GPU provides a guarantee for the real-time performance of deep learning. In this paper, the Faster-RCNN model is adopted to identify the precipitation clouds, and its block diagram is shown in Fig. 7.

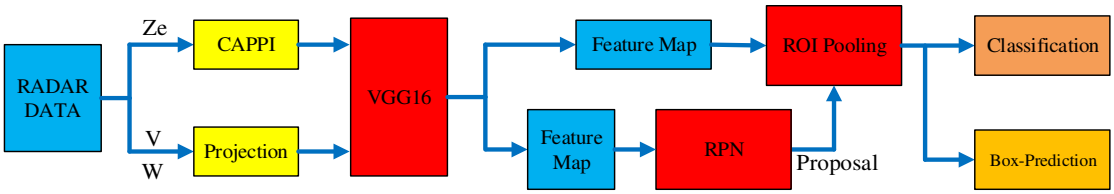

Fig. 7 The block diagram of precipitation clouds identification based on Faster-RCNN

Before identifying precipitation clouds, this paper preprocesses radar data, including CAPPI inversion of reflectivity, and radial projection of ground horizontal wind field, which are mentioned above. Faster-RCNN model is composed of Feature extraction, Region Proposal Networks (RPN) and Classification, which are described below.

3.3.1. Feature extraction

VGG-Net [34] is a classic deep learning network model, which has great advantages in CNN

feature extraction. In this algorithm, multiple 3×3 convolution layers and 2×2 pooling layers are used to extract features from the original data, and the performance of the model is improved by increasing the number of layers in the network. Moreover, the series of multiple small convolution kernels can be equivalent to a large scale convolution kernel, but the number of parameters in the network will be greatly reduced, and the nonlinear expression ability of the network will be enhanced. In this paper, the VGG16-Net is applied to extract features from radar data, and the architecture of the VGG16-Net used in this paper is shown in Fig. 8.

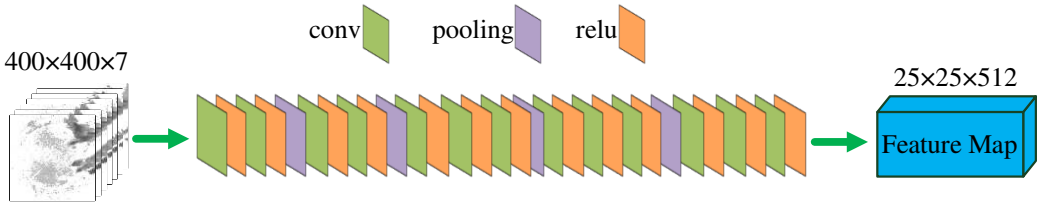

Fig. 8 The architecture of the VGG16-Net

Firstly, the input layer is a matrix with a size of $400\times400\times7$, where 400×400 corresponds to the coverage of radar data, and each resolution unit is $0.5\times0.5km^2$. Moreover, the input data includes three parts, which are CAPPI data of reflectivity with a size of $400\times400\times5$, the radial velocity data of the ground horizontal wind field with a size of 400×400, and the spectral width data of the ground horizontal wind field with a size of 400×400. Secondly, VGG16-Net is composed of 13 convolution layers and 4 pooling layers, and its detailed structure is shown in Table 3. Finally, the output layer is a Feature Map with a size of $25\times25\times512$, which reflects the spatial structure characteristics of the input data.

Table 3 The structure of VGG16-Net.

Layer	Kernal	Input	Output
Conv1(Conv2D)	(1,3,3,64)	(1,400, 400, 7)	(1,400,400,64)
Conv2(Conv2D)	(1,3,3,64)	(1,400, 400, 64)	(1,400,400,64)
maxPooling1	(2 ,2)	(1,400, 400, 64)	(1,200, 200, 64)
Conv3(Conv2D)	(1,3,3,128)	(1,200, 200, 64)	(1,200, 200,128)
Conv4(Conv2D)	(1,3,3,128)	(1,200,200,128)	(1,200, 200,128)
maxPooling2	(2 ,2)	(1,200,200,128)	(1,100,100,128)
Conv5(Conv2D)	(1,3,3,256)	(1,100,100, 128)	(1,100,100,256)
Conv6(Conv2D)	(1,3,3,256)	(1,100,100, 256)	(1,100,100,256)
Conv7(Conv2D)	(1,3,3,256)	(1,100,100, 256)	(1,100,100,256)

maxPooling3	(2 ,2)	(1,100,100, 256)	(1,50, 50, 256)
Conv8(Conv2D)	(1,3,3,512)	(1,50, 50, 256)	(1,50, 50,512)
Conv9(Conv2D)	(1,3,3,512)	(1,50, 50,512)	(1,50, 50,512)
maxPooling4	(2 ,2)	(1,50, 50,512)	(1,25,25,512)
Conv11(Conv2D)	(1,3,3,512)	(1,25,25,512)	(1,25,25,512)
Conv12(Conv2D)	(1,3,3,512)	(1,25,25,512)	(1,25,25,512)
Conv13(Conv2D)	(1,3,3,512)	(1,25,25,512)	(1,25,25,512)

3.3.2. RPN

Target detection algorithms based on CNN, such as R-CNN, Fast-RCNN and Faster-RCNN, have achieved good results in target detection in recent years [29-33]. R-CNN and Fast-RCNN adopt the selective search method to generate candidate regions, which have a large number of overlaps and are time-consuming, greatly reducing the detection efficiency of the model. Faster-RCNN used a neural network to generate candidate regions, namely RPN, which greatly improved the efficiency of target detection. The architecture of RPN is shown in Fig. 9.

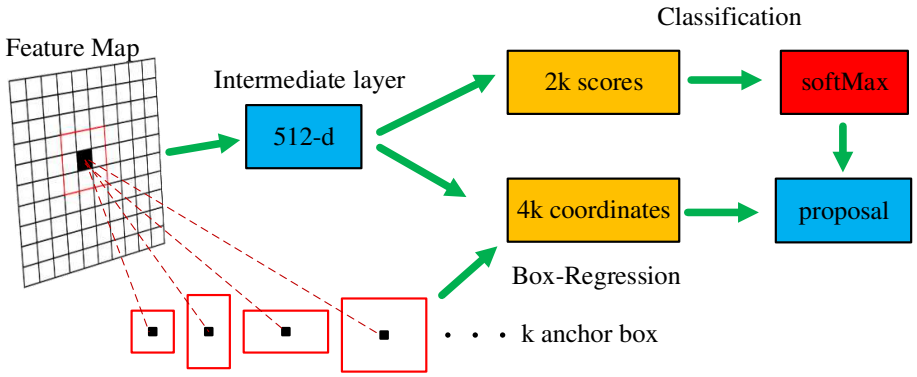

Fig. 9 The architecture of RPN

The detailed explanation of the RPN in Fig. 9 can be seen below:

1. The input data is a $25\times25\times512$ feature map, which is obtained by VGG16-Net.
2. To generate region proposals, we slide a small network over the input data. This network is fully connected to a 3 × 3 spatial window of the $25\times25\times512$ feature map. Moreover, each sliding window is mapped to a 512-d vector.
3. At each sliding-window location, we simultaneously predict k region proposals (where $k=9$). The 9 proposals are parameterized relative to 9 reference boxes, called anchors. Moreover, 9 anchors are generated by using 3 scales and 3 aspect ratios.
4. As described in (2), each region proposal can be mapped to a 512-d vector. Then, this vector

is fed into two sibling fully-connected layers, which are a box-regression layer and a box-classification layer. The box-classification layer gives the probability that this region proposal belongs to the foreground or background respectively. The box-regression layer gives the location information of this region proposal.

5. The outputs are 300 optimal region proposals, which are selected from a large number of region proposals by using the Non-Maximum Suppression method [35].

3.3.3. Classification

The architecture of classification is shown in Fig. 10. Each optimal region proposal is mapped to the $25\times25\times512$ feature map to obtain the corresponding feature expression. This feature expression is divided into 7×7 sub-blocks according to horizontal and vertical directions, and then each sub-block is maximally sampled to obtain a feature map with a size of 7×7. This process is called ROI Pooling [33].

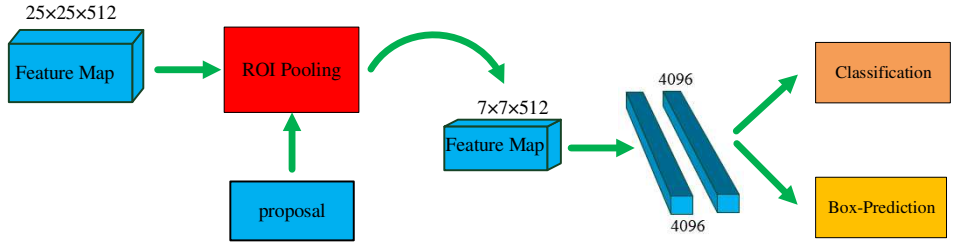

Fig. 10 The architecture of classification.

As shown in Fig. 10, any size region proposal can be normalized into a $7\times7\times512$ feature map by ROI Pooling. This $7\times7\times512$ feature map is fed into two consecutive fully-connected layers, resulting in a 1×4096 vector. Moreover, this vector is fed into two sibling fully-connected layers, which are a box-Prediction layer and a box-classification layer. The probability and position of the final target are given by the box-classification layer and box-Prediction layer respectively.

3.3.4. Training and Testing

As shown in Fig. 7, the Faster-RCNN model is composed of the detection network and the RPN network. Moreover, the two networks share the feature extraction module. The Alternating training method is applied to training the Faster-RCNN model, and it is derived from Reference [33]. The training process is as follows:

1. To train the RPN network, the Image-Net pre-training model was used to initialize the RPN network (except first convolutional layer, which was randomly initialized), and the number of

iterations was 10,000 times.

2. To train the detection network based on (1), the number of iterations was 10,000 times.
3. Fixed feature extraction module, fine-tuned parameters of non-shared layer in RPN network, and the number of iterations was 5000 times.
4. Fine-tuning the parameters of the non-shared layer in the detection network, and the number of iterations is 5000 times.

In this paper, the experimental environment with: NVIDIA Tesla P40 GPU, CUDA 9.1, Ubuntu 16.04, memory 24GB. Moreover, the development platform is Python+Tesorflow. The training set and testing set are described in Table 2. The test results show that the precision of identification results is 96%.

4 Results and discussions

In this paper, the performance of the precipitation clouds identification method is evaluated by the data detected in a mixed cloud precipitation process by using the CINRAD-SA dual-polarization Doppler weather radar which is upgraded in China. In order to verify the reliability of the identification method, we adopt the identification method proposed in Reference [12] to identify this case, and find that the identification results of the two methods are basically consistent.

On 19 March 2016, a heavy rainfall process was detected by the CINRAD-SA radar, which is located in Guangzhou, Guangdong, China (23°01′N, 113°35′E). The experimental data were detected from 12 continuous volume scan in the period from 2342UTC on March 19, 2016 to 0054UTC on March 20, 2016. Moreover, the interval time of adjacent volume scan is 6 minutes. The reflectivity CAPPI data are inverted by using the Adaptive Barnes interpolation method, which is introduced in section 3.1. Fig. 11(a) is the reflectivity CAPPI distribution map at 2-6km altitudes. The top of the Figure is the original CAPPI distribution map, and the bottom is the standardized CAPPI distribution map. The paper only processes the data in the area within 100 km. The data resolution is 500×500 meters, and the distance between adjacent circles is 25 km. Fig. 11(b) is the radial velocity distribution map of the ground horizontal wind field. Fig.11(c) is the spectral width data distribution map of the ground horizontal wind field. Each Figure contains two parts, the original distribution map on the left, and the standardized distribution map on the right.

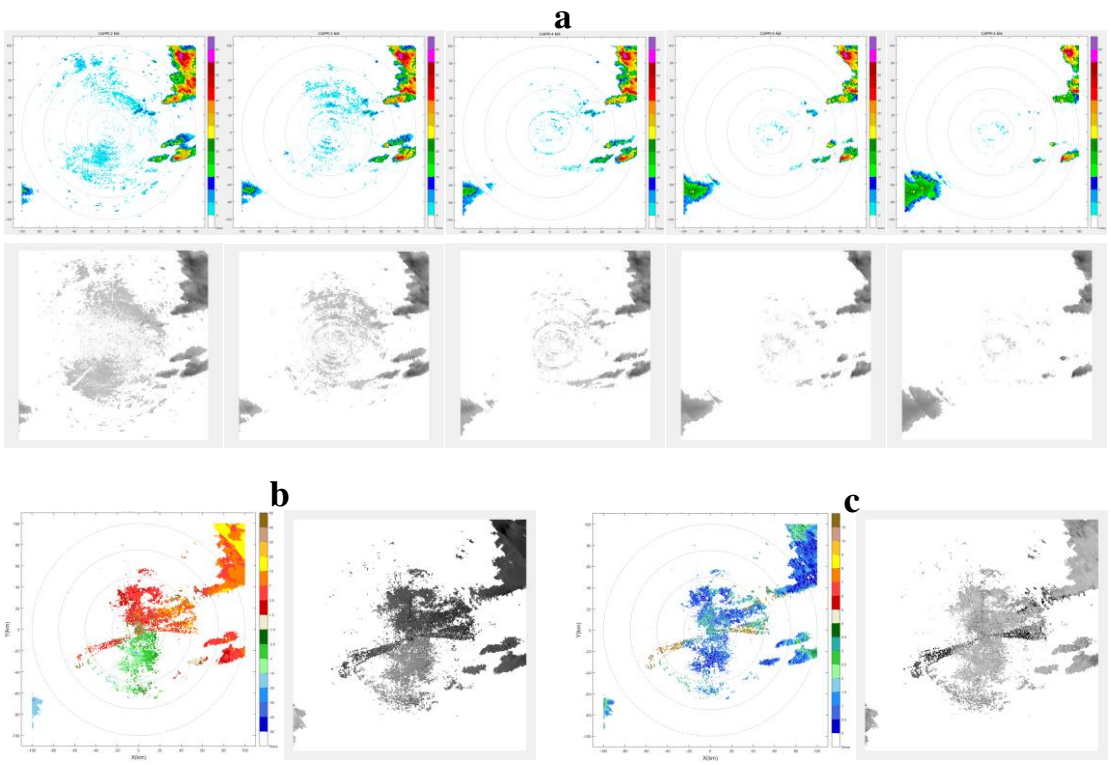

Fig. 11 The pre-processed radar data corresponding to 2342UTC, **a** CAPPI distribution map of the reflectivity at 2-6 Km altitudes, **b** Radial velocity distribution map of the ground horizontal wind field, **c** Spectral width data distribution map of the ground horizontal wind field.

As shown in Fig. 11(a), the red area on northeast of the radar station is a heavy precipitation area. The reflectivity value of this area reaches over 40dbZ, and the reflectivity center reaches 60dbZ. In the horizontal direction, the radar reflectivity decreases gradually with the outward direction of the reflectivity center, and the reflectivity value at 20 kilometers away from the reflectivity center decreases to 30dbZ. It reflects that the reflectivity of this region has a large gradient in the horizontal direction. In the vertical direction, the radar reflectivity reaches its maximum value at the height of 3km. As the height increases or decreases, the reflectivity will gradually decreases, which reflects that the reflectivity of this region also has a large gradient in the vertical direction.

As shown in Fig. 11(b), the left side of the radar station is southeast wind, and the right side is southwest wind. It is accompanied by slight convergence. As described in section 3.2, it can be inferred that this time is the middle and late period of convective cloud precipitation. The radial velocity has obvious abrupt change in the heavy precipitation area above mentioned. Moreover, the radial velocity decreases gradually when it closes to the precipitation center. In Fig. 11(c), the

spectral width data of this heavy precipitation area gradually increases when it closes to the precipitation center. Combined with the characteristics above mentioned, the precipitation cloud corresponding to the heavy precipitation region should be convective cloud. Fig. 12(a) shows the identification result of Faster-RCNN model. It can be seen that the identification results are basically consistent with the analyses above.

Reference [12] proposes six preparative reflectivity morphological parameters for identifying precipitation clouds, includes composite reflectivity and its horizontal gradient, echo top height associated with 35 dBZ reflectivity and its horizontal gradient, vertically integrated liquid water content and its density, which are based on the differences of radar reflectivity distribution morphology between convective and stratiform clouds. Moreover, the fuzzy logic method is applied to identify the precipitation cloud based on the distribution law of each parameter. This identification method has been widely used in China. We use this method to identify the precipitation clouds at 2342UTC, and the identification results are shown in Fig. 12(b). The red areas in the Figure are convective clouds, and other precipitation cloud areas are stratiform clouds by default.

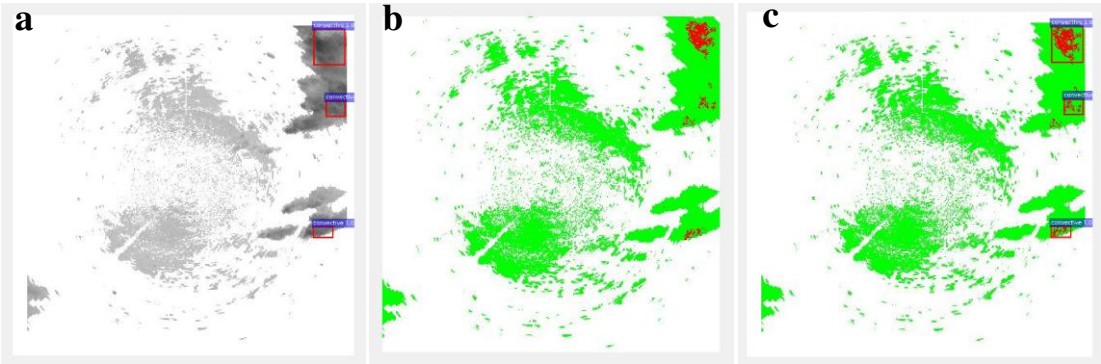

Fig. 12 The identification result of precipitation clouds corresponding to 2342UTC, **a** Faster-RCNN, **b** Traditional method, **c** comparison.

The identification results of the two methods are compared, and the comparison results are shown in Fig. 12(c). The red box corresponds to the convective cloud box in Fig. 12(a). Moreover, the red area corresponds to the convective cloud in Fig. 12(b). It can be seen that the identification results of the two methods are basically consistent. In addition, the above two methods are used to identify the precipitation clouds corresponding to the 12 continuous volume scan data. The identification results are shown in Fig. 13.

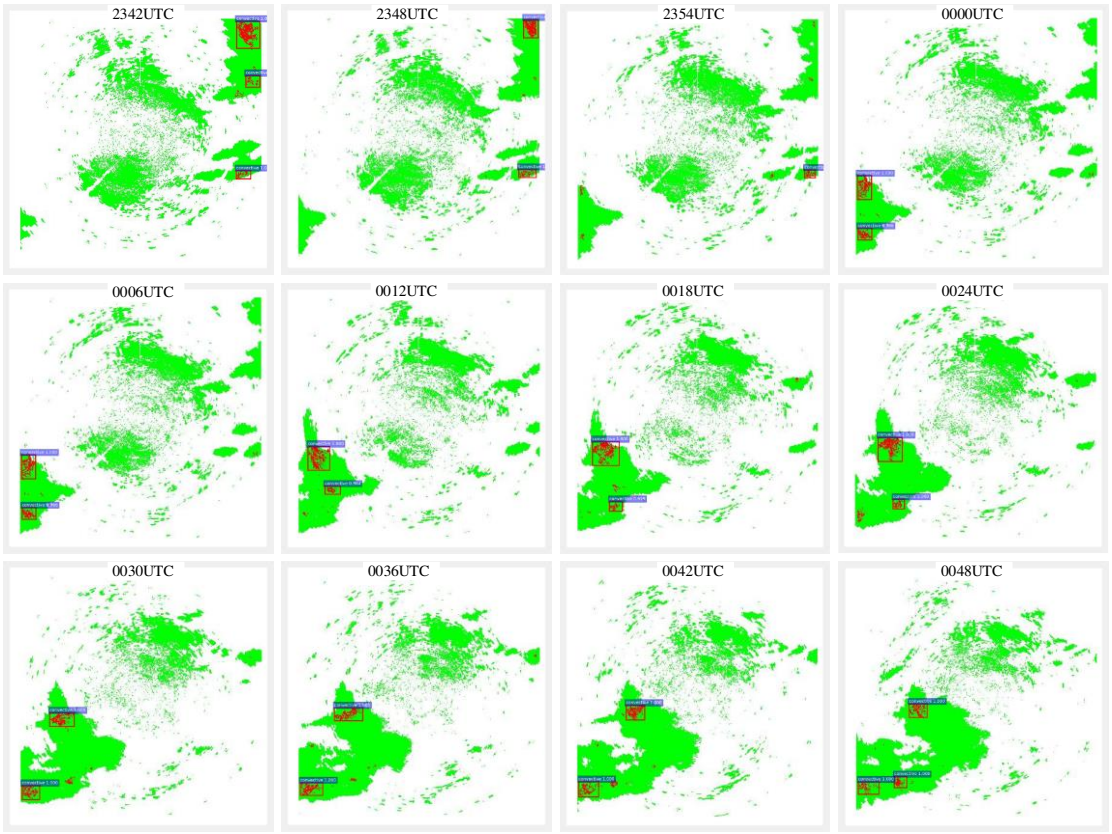

Fig. 13 The identification results of precipitation clouds corresponding to 2342UTC-0054UTC

Table 4 The comparison results of identification methods

Method	Time	Recall	Precision
Proposed in this paper	11s	85.2%	96%
Traditional	32s	90%	72%

As shown in Fig. 13，the identification results of the two methods are basically consistent. Moreover, the testing set in Table 2 is used in the evaluation of the two identification methods, and the evaluation results are shown in Table 4. It can be seen that the traditional methods have higher recall rate, but poor accuracy. However, the new identification method proposed in this paper has great advantages in efficiency and accuracy.

5 Conclusions

With continued threat from severe convection weather, the identification of precipitation clouds is crucial to weather forecast and aviation meteorology. Traditional identification methods utilize some parameters calculated from radar reflectivity to identify the precipitation clouds, which are based on the differences of radar reflectivity distribution morphology between strati-form and convective clouds in three-dimensional space. These methods have a common shortcoming that

the radial velocity data detected by Doppler Weather Radar has not been applied to the identification of precipitation clouds because it is insensitive to the convective movement in the vertical direction. However, the convective movement in the vertical direction is an important feature for precipitation clouds identification. Section 3.2 draws the conclusion that the ground horizontal wind field is often accompanied by convergence and divergence during the growth and mature stages of convective cells. Moreover, the radial velocity detected by the Doppler weather radar at minimum elevation can be regarded as the projection of horizontal wind field on the radar radial direction. Therefore, the radial velocity data detected by the Doppler weather radar at minimum elevation can be used to the identification of precipitation clouds.

In this paper, a new method for precipitation clouds identification was described, which makes full use of the data products of Doppler weather radar, including reflectivity, radial velocity and spectrum width of radial velocity. Firstly, the adaptive Barnes interpolation method is used to interpolate the radar scanning volume data to obtain the reflectivity CAPPI data at multiple altitudes. Secondly, the radial velocity and the spectral width of the horizontal wind field on the ground are respectively obtained by the projection of the radar detection data at the minimum elevation, which reflect the formation and development of convective motion. Finally, the Faster-RCNN algorithm was applied to identify the precipitation clouds based on the data above mentioned. Experiments to evaluate the proposed method showed that the new method has great advantages in efficiency and accuracy compared with the traditional methods.

This study is the first one that reports applying the radial velocity data detected by the Doppler weather radar to the identification of precipitation clouds. Moreover, the deep learning algorithm was applied to identify the precipitation clouds. Compared with traditional identification methods, this method achieves better results in efficiency and accuracy. However, the training process of Faster-RCNN model usually requires large labeled data and powerful computational resources. It is obvious that the training samples described in section 3.2 are insufficient. Future work should be focused on collecting more samples for training and testing of the Faster- RCNN model. Moreover, Future work should minimize the running time of the precipitation clouds identification system by optimizing the internal algorithms.

Availability of data and materials

The datasets supporting the conclusions of this article are private, and it came from the CMA Key Laboratory of Atmospheric Sounding, Chengdu, Sichuan, China.

Competing interests

The authors declare that they have no competing interests.

Fundings

This research was funded by the National Natural Science Foundation of China (Joint Fund of Civil Aviation Research, award number U1733103).

Authors' contributions

HW conceived the study. YR designed the study and wrote the manuscript. JW marked the samples. LT collected the data and revised the manuscript. XL drew the figures and improved the structure of the manuscript. All authors read and approved the final manuscript.

Acknowledgements

We would like to sincerely thank to the workmates of CMA Key Laboratory of Atmospheric Sounding, locating in Chengdu University of Information Technology, including the teachers, Xu Wang, and Tao Liu, for their help.

Authors Information

YR received the M.S. degree in signal and information processing from Chengdu University of Information Technology, Sichuan, China, in 2019. Now he is an Atmospheric Sounding Engineer at Fuling Meteorological Bureau, Chongqing, China. His research interest includes the weather radar signal processing and machine learning.

HW received the Ph.D. degree in signal and information processing from University of Electronic Science and Technology of China, Sichuan, China, in 2008. He is now a Full Professor with the School of Electronic Engineering, Chengdu University of Information Technology, Sichuan, China. His research interests include weather radar signal processing, dual-polarization Doppler weather radar data analysis and processing, and SAR image processing.

LT received the B.S. degree in atmospheric science from Chengdu University of Information Technology, Sichuan, China, in 2009. Now she is an Atmospheric Sounding Engineer at Fuling Meteorological Bureau, Chongqing, China.

JW received the B.S. degree in atmospheric science from Chengdu University of Information Technology, Sichuan, China, in 2010. Now he is an Atmospheric Sounding Engineer at Fuling Meteorological Bureau, Chongqing, China.

XL received the M.S. degree in communication and information system from Shandong University, Shandong, China, in 2010. Now she is a teacher at Physics Science and Information Engineering College, Liaocheng University, Shandong, China.

References

[1] Brown R A. Doppler Weather Radar[M]// Encyclopedia of Natural Hazards. 2013.

[2] Schuur T, Ryzhkov A, Heinselman P, et al. Observations and Classification of Echoes with the Polarimetric WSR-88D radar[J]. 2003.

[3] Evans J, Turnbull D. Development of an automated windshear detection system using Doppler weather radar[J]. Proceedings of the IEEE, 1989, 77(11):1661-1673.

[4] Bringi V N, Chandrasekar V. Polarimetric Doppler weather radar: principles and applica-tions[J]. Atmospheric Research, 2002, 63(1):159-160.

[5] Zhang Z, Zheng G, Wei M, et al. Research on the system of advanced X-band Doppler weather radar with dual-linear polarization capability[C]//Advanced Computational Intelli-gence (ICACI), 2012 IEEE Fifth International Conference on. IEEE, 2012: 739-741.

[6] Hershberger J, Pratt T, Kossler R. Automated calibration of a dual-polarized SDR ra-dar[C]// Antenna Measurements & Applications. IEEE, 2017.

[7] Austin P M , Bemis A C . a Quantitative Study of the `BRIGHT Band' in Radar Precipitation Echoes[J]. Journal of the Atmospheric Sciences, 1950, 7(2):145-151.

[8] Robert A, Houze Jr. A Climatological Study of Vertical Transports by Cumulus-Scale Convection[J]. Journal of the Atmospheric Sciences, 1973, 30(6):1112-1123.

[9] Churchill D D , Jr R A H . Development and Structure of Winter Monsoon Cloud Clusters On 10 December 1978[J]. J.atmos.sci, 1992, 41(6):933-960.

[10] Steiner M , Houze R A , Yuter S E . Climatological characterization of three-dimensional storm structure from operational radar and rain gauge data[J]. Journal of Applied Meteorology, 1995, 34(9):1978-2007.

[11] Biggerstaff M I , Listemaa S A . An improved scheme for convective/stratiform echo classification using radar reflectivity[J]. Journal of Applied Meteorology, 1985, 39(12):2129-2150.

[12] Xiao Yanjiao, Liu Liping . Identification of Stratiform and Convective Cloud Using 3D Radar Reflectivity Data[J].Chinese Journal of Atmospheric Sciences, 2007, 31(4):645-654.

[13] Bousquet O , Chong M . A Multiple-Doppler Synthesis and Continuity Adjustment Tech-nique (MUSCAT) to Recover Wind Components from Doppler Radar Measurements[J]. Journal of Atmospheric and Oceanic Technology, 1998, 15(2):343-359.

[14] Dowell D C , Shapiro A . Stability of an Iterative Dual-Doppler Wind Synthesis in Cartesian Coordinates[J]. Journal of Atmospheric and Oceanic Technology, 2003, 20(11):1552-1559.

[15] Rutledge S A, Petersen W A. Vertical Radar Reflectivity Structure and Cloud-to-Ground Lightning in the Stratiform Region of MCSs: Further Evidence for In Situ Charging in the Stratiform Region[J]. Monthly Weather Review, 1994, 122(8):1760.

[16] Matrosov S Y, Uttal T, Hazen D A. Evaluation of Radar Reflectivity Based Estimates of Water Content in Stratiform Marine Clouds.[J]. Journal of Applied Meteorology, 2004, 43(43):405-419.

[17] Kumar S, Bhat G S. Vertical structure of radar reflectivity in deep intense convective clouds over the tropics[C]// Noaa Satelite Cnference. 2016.

[18] Pauley P M , Wu X . The Theoretical, Discrete, and Actual Response of the Barnes Ob-jective Analysis Scheme for One- and Two-Dimensional Fields[J]. Monthly Weather Review, 1990, 118(5):1145-1164.

[19] Yun-Xian H , Ying Z . Comparison of Interpolation Schemes for the Doppler Weather Radar Data[J]. Remote Sensing Information, 2008, 21(2):39-45.

[20] Rosenfeld D, Mintz Y. Evaporation of Rain Falling from Convective Clouds as Derived from Radar Measurements.[J]. Journal of Applied Meteorology & Climatology, 1988, 27(3):209-215.

[21] Illingworth, Anthony J . The formation of rain in convective clouds[J]. Nature, 1988, 336(6201):754-756.

[22] Chen C L P. Deep learning for pattern learning and recognition[C]//Applied Computa-tional Intelligence and Informatics (SACI), 2015 IEEE 10th Jubilee International Symposium on. IEEE, 2015: 17-17.

[23] Lecun Y, Bengio Y, Hinton G. Deep learning[J]. Nature, 2015, 521(7553):436-444.

[24] Schmidhuber J. Deep learning in neural networks: an overview[J]. Neural Networks the Official Journal of the International Neural Network Society, 2014, 61:85-117.

[25] Felzenszwalb P, Mcallester D, Ramanan D. A discriminatively trained, multiscale, de-formable part model[C]// IEEE Conference on Computer Vision & Pattern Recognition. 2008.

[26] Sun Y , Wang X , Tang X . Deep Convolutional Network Cascade for Facial Point Detection[C]// Computer Vision and Pattern Recognition (CVPR), 2013 IEEE Conference on. IEEE, 2013.

[27] Yan J, Zhen L, Wen L, et al. The Fastest Deformable Part Model for Object Detec-tion[C]// Computer Vision & Pattern Recognition. 2014.

[28] Sermanet P , Eigen D , Zhang X , et al. OverFeat: Integrated Recognition, Localization and Detection using Convolutional Networks[J]. Eprint Arxiv, 2013.

[29] Krizhevsky A , Sutskever I , Hinton G . ImageNet Classification with Deep Convolutional Neural Networks[J]. Advances in neural information processing systems, 2012, 25(2).

[30] Girshick R , Donahue J , Darrell T , et al. Rich Feature Hierarchies for Accurate Object Detection and Semantic Segmentation[C]// 2014 IEEE Conference on Computer Vision and Pattern Recognition (CVPR). IEEE Computer Society, 2014.

[31] He K , Zhang X , Ren S , et al. Spatial Pyramid Pooling in Deep Convolutional Networks for Visual Recognition[J]. IEEE Transactions on Pattern Analysis & Machine Intelligence, 2014, 37(9):1904-16.

[32] Girshick R. Fast R-CNN[J]. Computer Science, 2015.

[33] Ren S, He K, Girshick R, et al. Faster R-CNN: towards real-time object detection with region proposal networks[C]// International Conference on Neural Information Processing Systems. 2015.

[34] Simonyan K , Zisserman A . Very Deep Convolutional Networks for Large-Scale Image Recognition[J]. Computer Science, 2014.

[35] Neubeck A , Gool L J V . Efficient Non-Maximum Suppression[C]// 18th International Conference on Pattern Recognition (ICPR 2006), 20-24 August 2006, Hong Kong, China. IEEE Computer Society, 2006.

Figures

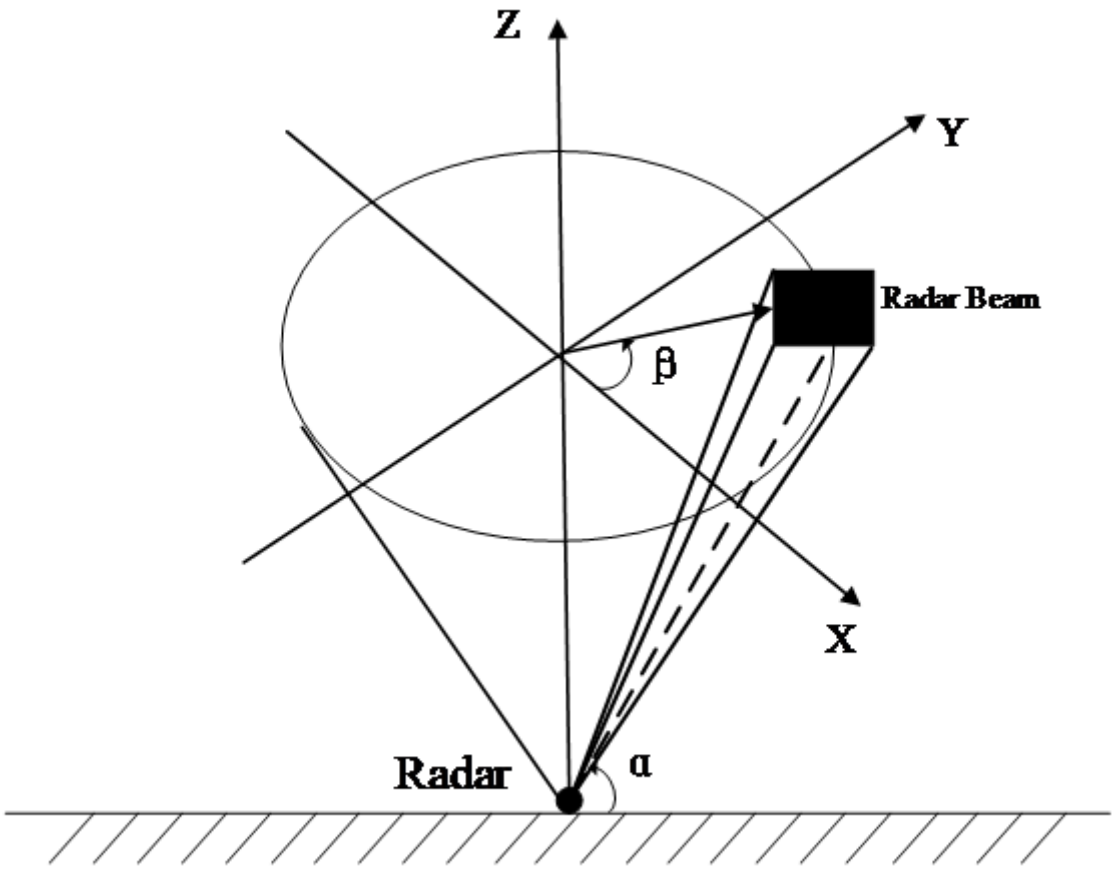

Figure 1

The schematic diagram of PPI scan mode

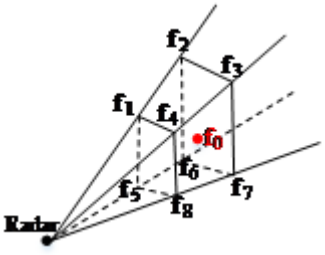

Figure 2

An illustration of Adaptive Barnes interpolation.

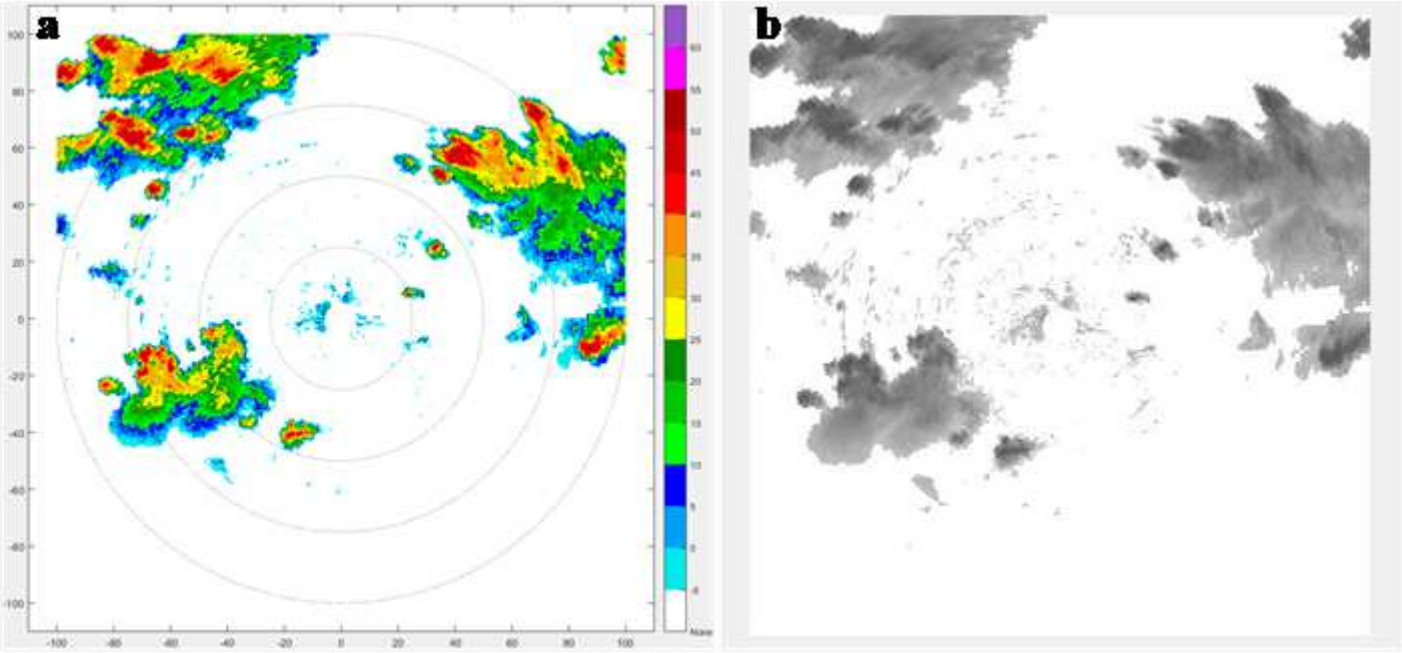

Figure 3

Standardization of radar reflectivity CAPPI data, a origin, b Standardization

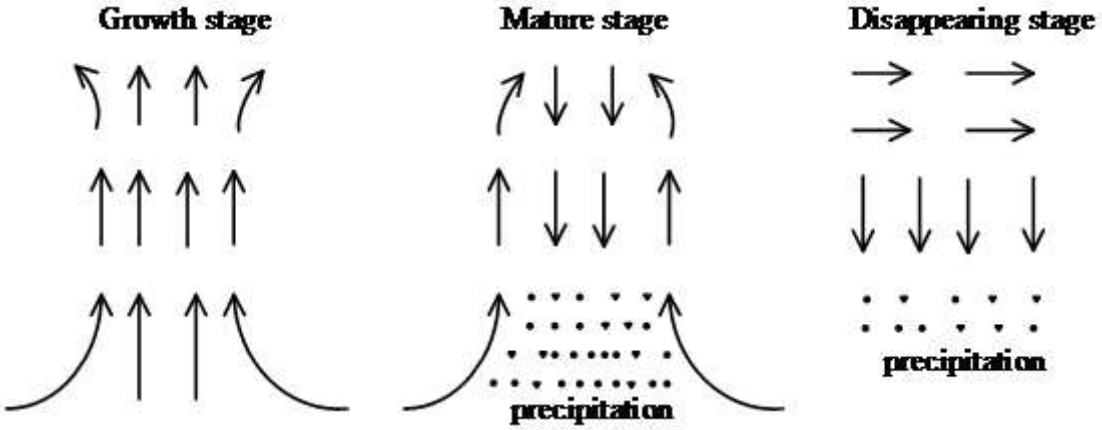

Figure 4

The evolution process of convective cells

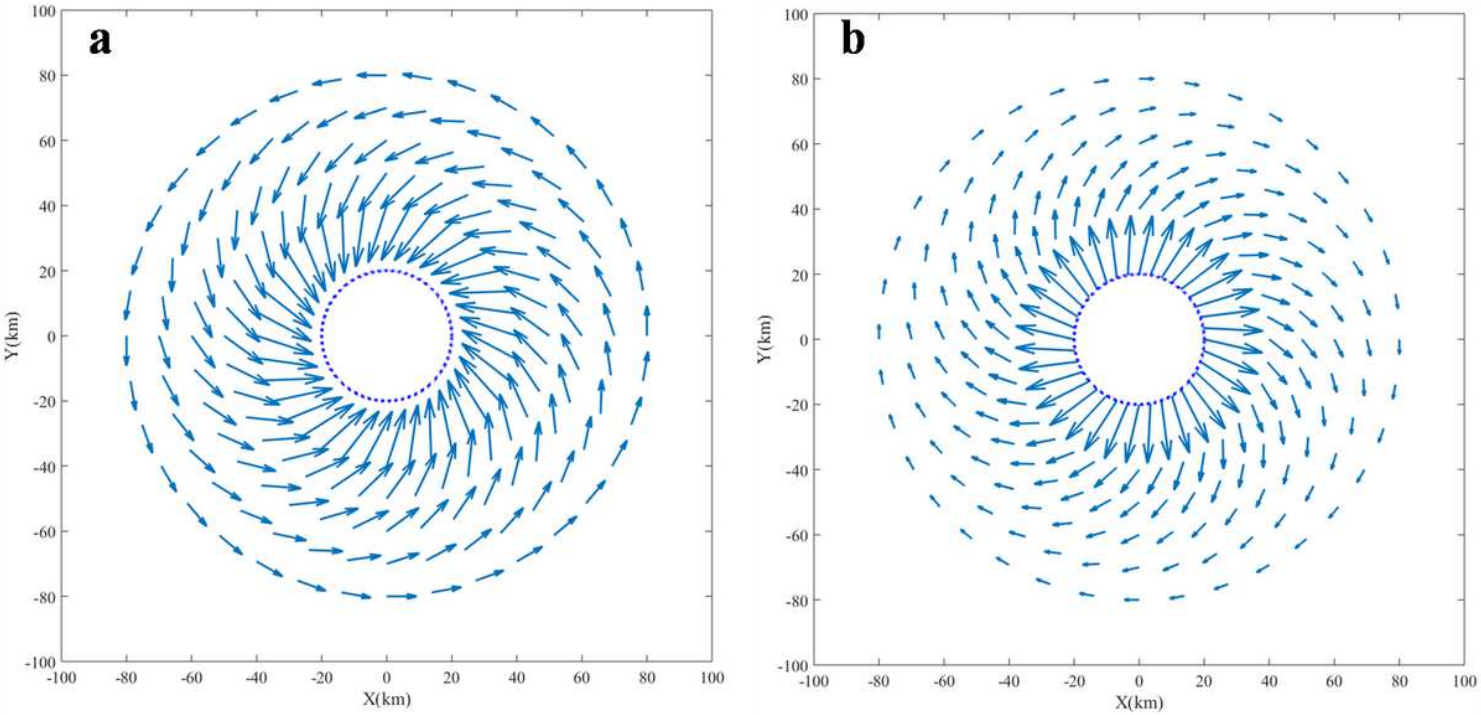

Figure 5

Simulation diagram of ground wind field, a convergence, b divergence

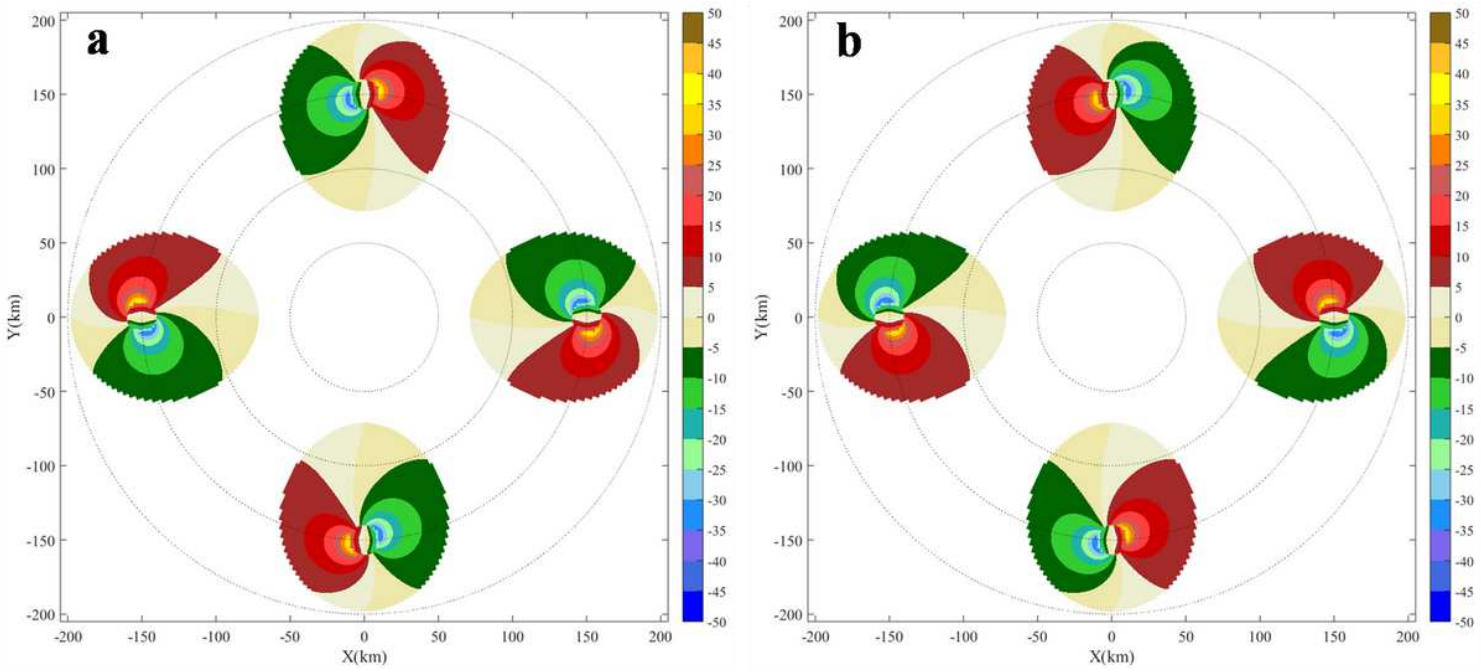

Figure 6

The PPI distribution of the radar radial velocity data corresponding to a convergence and b divergence

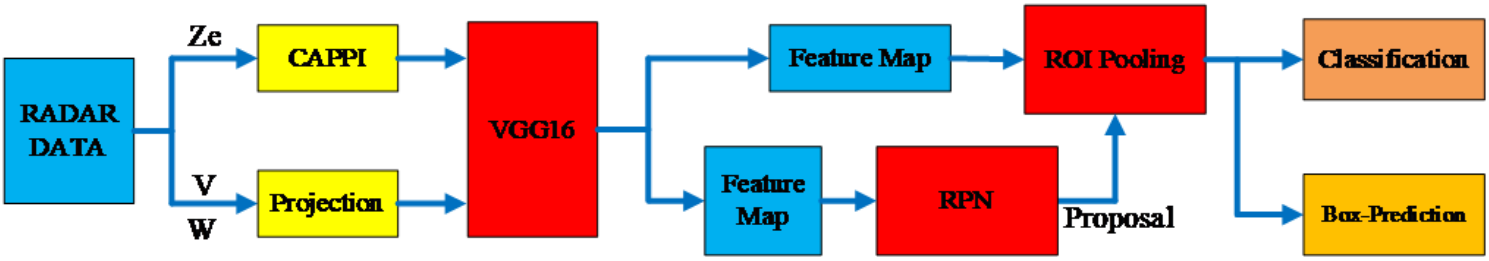

Figure 7

The block diagram of precipitation clouds identification based on Faster-RCNN

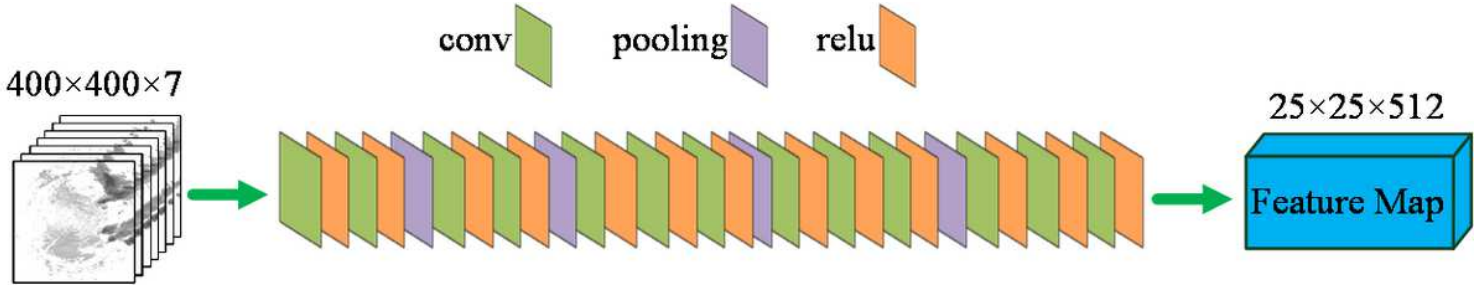

Figure 8

The architecture of the VGG16-Net

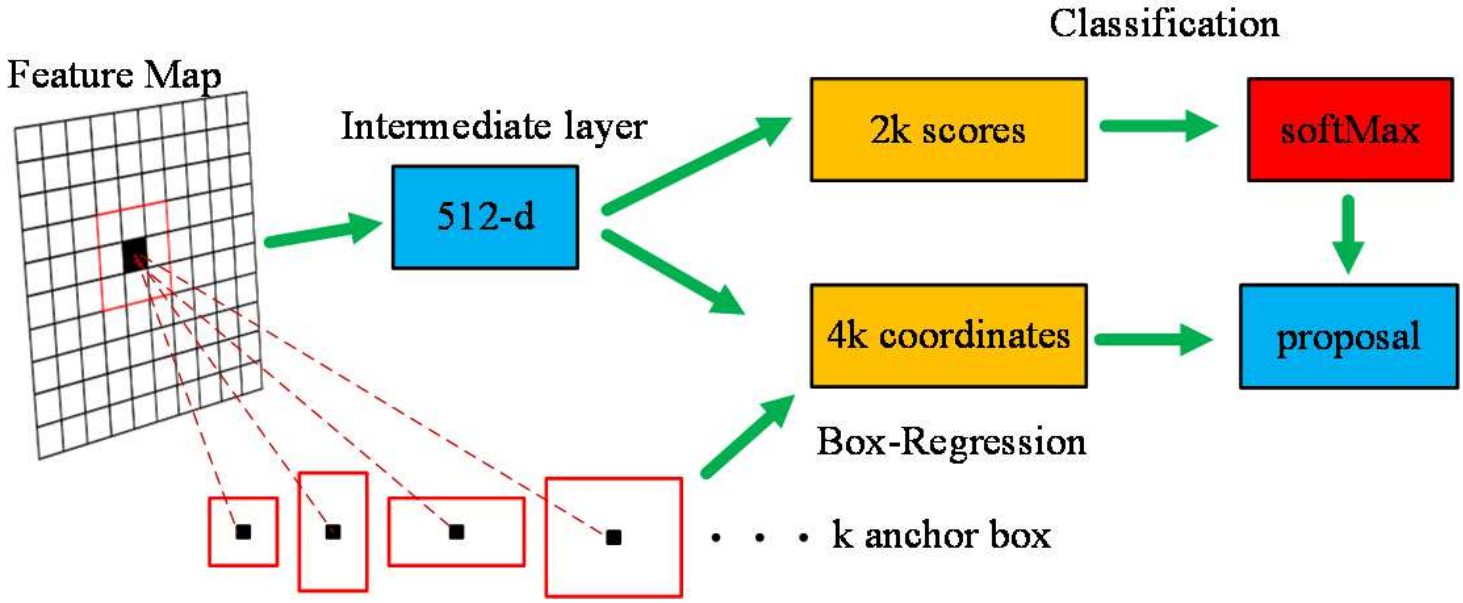

Figure 9

The architecture of RPN

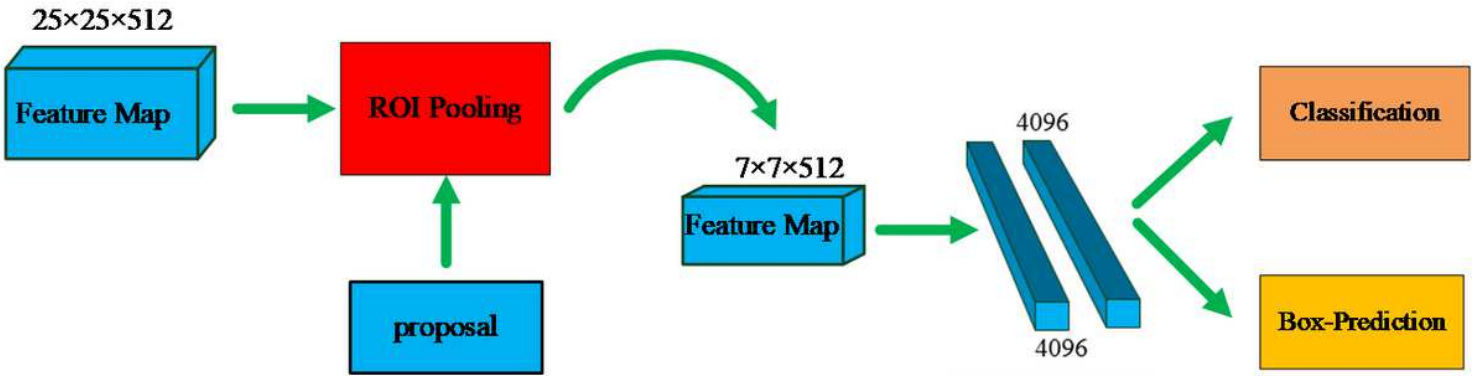

Figure 10

The architecture of classification.

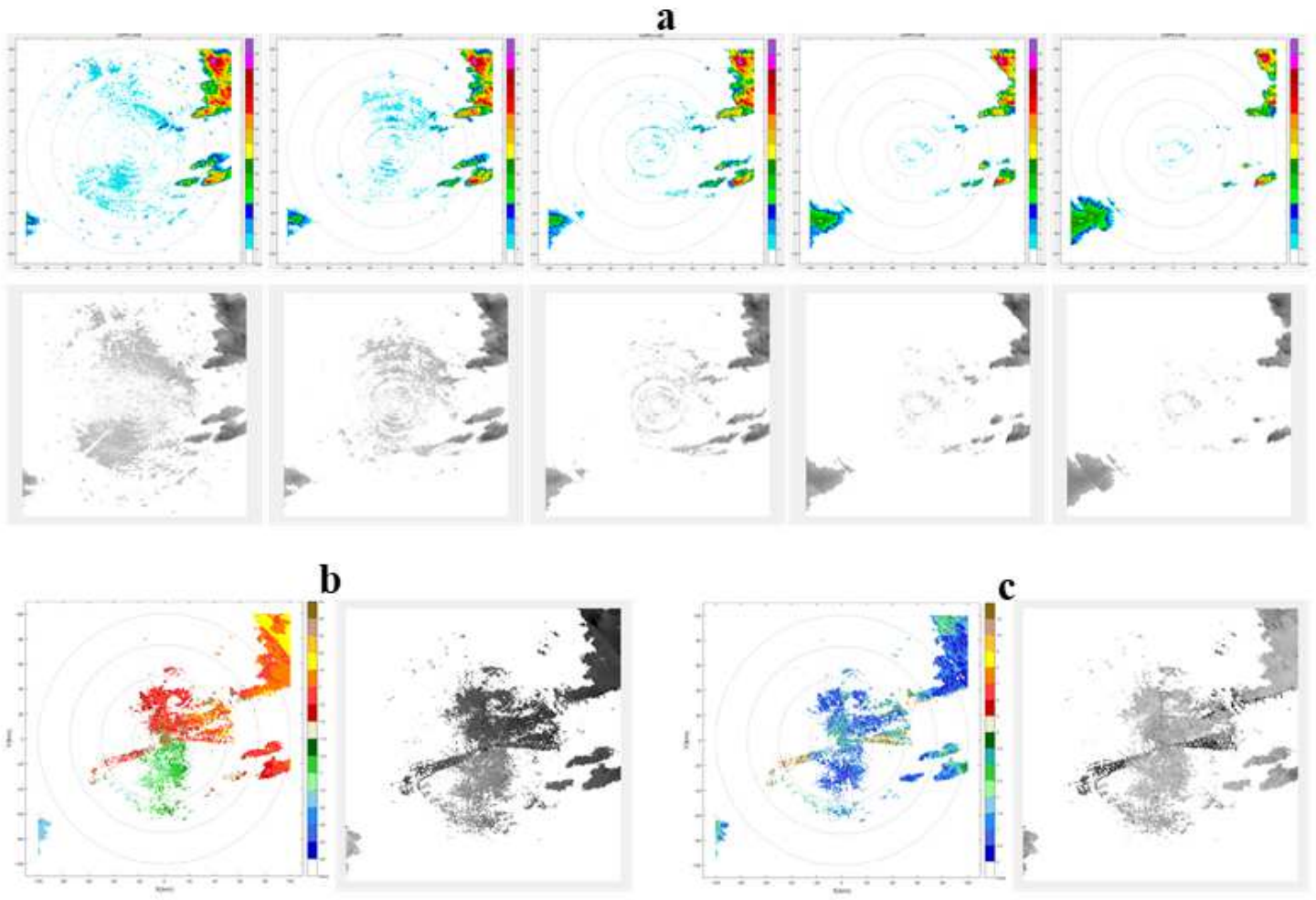

Figure 11

The pre-processed radar data corresponding to 2342UTC, a CAPPI distribution map of the reflectivity at 2-6 Km altitudes, b Radial velocity distribution map of the ground horizontal wind field, c Spectral width data distribution map of the ground horizontal wind field.

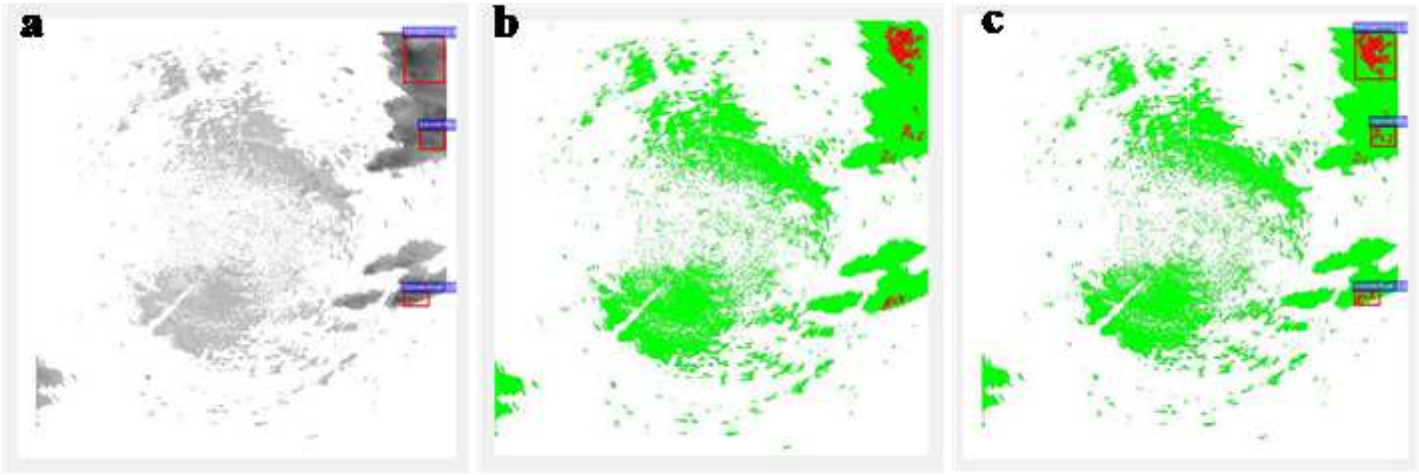

Figure 12

The identification result of precipitation clouds corresponding to 2342UTC, a Faster-RCNN, b Traditional method, c comparison.

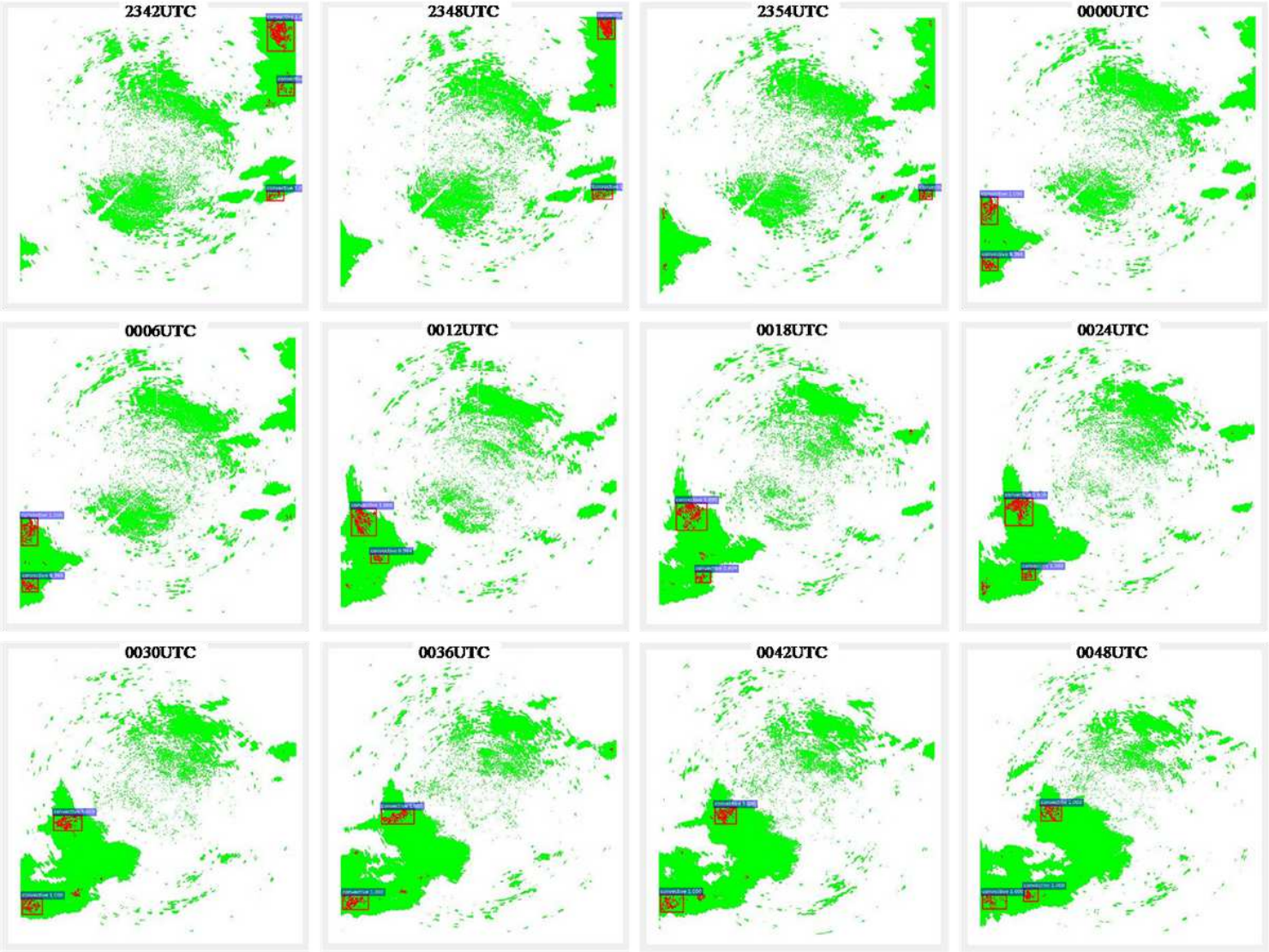

Figure 13

The identification results of precipitation clouds corresponding to 2342UTC-0054UTC